ACS APPLIED MATERIALS & INTERFACES

Research Article

www.acsami.org

Synthesis of Ultrafine Pt Nanoparticles Stabilized by Pristine Graphene Nanosheets for Electro-oxidation of Methanol

Yi Shen,*[,†] Zhihui Zhang,[†] Ranran Long,[†] Kaijun Xiao,[†] and Jingyu Xi*[,‡]

[†]College of Light Industry and Food Sciences, South China University of Technology, Guangzhou 510640, China

[‡]Lab of Advanced Power Sources, Graduate School at Shenzhen, Tsinghua University , Shenzhen 518055, China

Supporting Information

ABSTRACT: In this study, the pristine graphene nanosheets (GNS) derived from chemical vapor deposition process were employed as catalyst support. In spite of the extremely hydrophobic GNS surface, ultrafine Pt nanoparticles (NPs) were successfully assembled on the GNS through a surfactant-free solution process. The evolution of Pt NPs in the GNS support was studied using transmission electron microscopy. It was found that the high-energy surface sites in the GNS, such as edges and defects, played a critical role on anchoring and stabilizing Pt nuclei, leading to the formation of Pt NPs on the GNS support. The concentration of the Pt precursor, i.e., H_2PtCl_6 solution had significant effects on the morphology of Pt/GNS hybrids. The resulting Pt/GNS hybrids were examined as catalysts for methanol electro-oxidation. It was indicated that the electrochemical active surface area and catalytic activity of the Pt/GNS hybrids were highly dependent on Pt loadings. The superior activity of the catalysts with low Pt loadings was attributed to the presence of Pt subnanoclusters as well as the strong chemical interaction of Pt NPs with the GNS support.

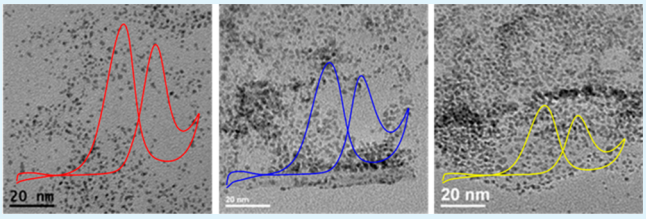

KEYWORDS: *direct methanol fuel cells, Pt ultrafine nanoparticles, graphene nanosheets, catalyst support effects, electro-catalysts, polyol-assisted synthesis*

1. INTRODUCTION

With increasing energy demand and great concern on environmental issues, direct methanol fuel cells (DMFCs) have attracted extensive attention as new power sources for mobile and portable electronic devices because of the high energy efficiency, low pollution emission, and operating temperature.[1] However, two critical issues, i.e., methanol crossover in electrolyte membranes and sluggish kinetics of methanol oxidation, still remain the obstacles for the commercialization of DMFCs.[2] For the first problem, many efforts have been directed in developing novel proton exchange membranes with enhanced proton/methanol selectivity.[3] To address the second issue, one strategy is to design bimetallic catalysts such as PtNi,[4] PtCo,[5] PtFe,[6] PtRu,[7,8] and PtPd[9] with enhanced catalytic activities, based on the so-called bifunctional and/or ligand effects. In addition, the selection of supporting material and further control of the dispersion and morphology of active component on the support also play an important role on the activity of catalysts.[10] For the application in DMFCs, noble metals with ultrafine sizes are highly desirable because of the increased surface area and the large number of edge and corner atoms, which greatly enhance the mass activity.[10] Nevertheless, the high surface energy associated with the ultrafine particles always leads to serious aggregation. Thus, an ideal catalyst support in DMFCs should not only exhibit a large surface area and excellent conductivity to facilitate the transport of reactants and electrons, but also interact with the active component to avoid aggregation.[11]

Currently, carbon materials, such as carbon black,[12] ordered mesoporous carbon,[13] carbon nanotubes,[14,15] carbon nanofibers,[16] and graphene,[17,18] are utilized as catalyst supports in fuel cells.[19−21] Recently, graphene nanosheets (GNS) have been of particular interest because of the high conductivity, large theoretical surface area, and unique graphitized basal plane.[22,23] Various GNS-based hybrids have been studied as catalysts in fuel cells.[24−30] It was found that Pt nanoparticles (NPs) supported on GNS showed high catalytic activity in DMFCs.[31] For instance, Yoo et al.[32] synthesized the Pt NPs stabilized by GNS and observed significant enhancement on activity toward methanol oxidation as compared with the commercial catalyst. It was proposed that the superior activity of the GNS-based catalyst was arisen from the modifications on the electronic structures of Pt NPs through the chemical interaction between the Pt NPs and GNS. Sharma et al.[33] synthesized Pt NPs supported on reduced graphene oxide (Pt/RGO). The Pt/RGO hybrids exhibited remarkable CO tolerance for methanol oxidation, resulting from the synergetic effects between the oxygen-containing groups on the RGO support and Pt NPs.

In the literature, the GNS supports were mostly commonly synthesized from the reduction of exfoliated graphite oxide and contained abundant functional groups such as hydroxyl,

Received: May 27, 2014
Accepted: August 21, 2014
Published: August 21, 2014

carbonyl and carboxyl.[34−37] These oxygen-containing groups play an important role on anchoring and stabilizing Pt NPs. However, the presence of these groups also inevitably interrupts the intrinsic structures of GNS and adversely affected the conductivity and stability of the GNS support.[38] In contrast to reduced graphene oxide, the graphene derived from chemical vapor deposition (CVD) contains less oxygen-containing groups and possesses higher conductivity and stability.[39] The GNS derived from CVD process at high temperatures is hydrophobic, which is commonly considered to be detrimental to the dispersion and immobilization of Pt NPs.[26] Nevertheless, it was demonstrated from this study that the GNS derived from CVD process could serve as an effective catalyst support in spite of the hydrophobic surface and that ultrafine Pt NPs could be assembled on the GNS support through the facile polyol-assisted reduction process. The high-energy surface sites in the GNS support, such as edges and defects played a critical role on the immobilization of Pt NPs. The morphology of Pt NPs was closely related to the ratio of GNS and Pt precursor. The resulting Pt/GNS hybrids were examined as catalysts for methanol electro-oxidation. It was found that the catalytic activity of the Pt/GNS catalyst was highly dependent on Pt loadings in the catalysts.

2. EXPERIMENTAL SECTION

2.1. Synthesis of GNS Support. The GNS support was prepared by CVD and further purified by acid etching and sedimentation separation, as described in our previous work.[40] The GNS consisted of few-layered graphene sheets (<10 layers). The surface area of the GNS was 247 m^2 g^{-1} as determined by the Brunauer−Emmett−Teller (BET) method.

2.2. Synthesis of Pt/GNS Catalysts. The Pt/GNS catalyst was synthesized using the polyol-assisted reduction method. The details of the experimental procedures are as follows: 100 mg of GNS support was dispersed into 150 mL of ethylene glycol by alternative ultrasonication and magnetic stirring to form a stable suspension. 1.2 g of NaOH was added into the mixture. After the complete dissolution of NaOH, a predetermined volume of H_2PtCl_6 aqueous solution (8 wt %) was also added into the mixture. Subsequently, the mixture was transferred into a hot oil bath and the reduction was carried out at 180 °C for 15 min under continuous magnetic stirring. After cooling to room temperature, the mixture was separated by centrifuge and thoroughly washed with ethanol. The resulting catalyst was dried at 80 °C overnight in a vacuum oven. Three catalyst samples with nominal Pt weigh percentages of 20, 40, and 60% were prepared, which were denoted as Pt 20%/GNS, Pt 40%/GNS, and Pt 60%/GNS, respectively.

2.3. Physical Characterization. A transmission electron microscope (JEM2010, JEOL) were used to observe the morphology of the samples. High-resolution TEM micrographs were obtained from an alternative JEM-2010F (JEOL) microscope. An energy dispersive X-ray (EDX) analyzer equipped in the TEM and an axis-ultra X-ray photoelectron spectrometer (Kratos-Axis Ultra System) with monochromatized Al−Kα radiation were used to analyze the elemental composition of the samples. The actual Pt content in the Pt/GNS catalyst was analyzed by inductively coupled plasma (ICP) analysis.

2.4. Electrochemical Measurements. Electrochemical measurements were carried out using a three-electrode cell connected to a PARSTAT 2273 electrochemical station (AMETEK, Inc. USA.). A gold patch (effective area 1 × 1 cm) coated with a thin layer of catalyst ink was used as working electrode.[15] The catalyst ink was prepared by ultrasonication of catalyst powder in a solution of Nafion solution (5 wt %), ethylene glycol, isopropanol and water (volume ratio 1:9:15:75). The catalyst suspension was transferred to the gold patch using a pipet and then dried at 80 °C. The cover density of catalyst on the gold patch was ca. 200 $\mu g/cm^2$. A saturated calomel electrode (SCE) and Pt gauze (effective area 1 × 1 cm) were used as reference and counter electrodes, respectively. Cyclic voltammograms (CV) were recorded in the potential range −0.2 to 1.0 V at a scan rate of 50 mV s^{-1}. A solution of 1 M methanol and 1 M H_2SO_4 was used as electrolyte. The electrochemical active surface area (ECSA) of the catalyst was determined from the hydrogen absorption−desorption process in 1 M H_2SO_4 solution. The chronopotentiometric curves were obtained under an applied potential of 0.6 V. Before the test, the solution was saturated with N_2 gas for 20 min. Several activation scans were performed until reproducible voltammograms were obtained. Only the last voltammograms were used for comparing the catalytic activity of the specified catalysts. The measurements were conducted at 25 °C and all potentials in this study were referenced to the SCE.

3. RESULTS AND DISCUSSION

3.1. Morphology of GNS Support. The sizes of the GNS are in the micrometer scale as shown in Figure 1a. The

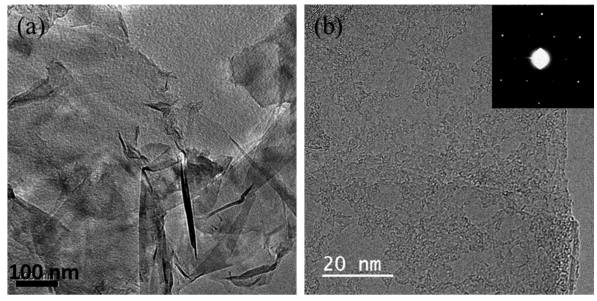

Figure 1. (a) TEM and (b) high-resolution TEM images of GNS derived from chemical vapor deposition (inset in b: selected area electron diffraction pattern of GNS).

stretched black regions in the micrograph are indicative of the scrolls and folds of the GNS. It is shown from the high-resolution TEM micrographs (Figure 1b) that many edges and defects are present in the GNS support due to the incomplete formation of intact graphene layers. To further verify the presence of edges and defects in the GNS, we conducted Raman tests as shown in Figure S1 in the Supporting Information. It was shown that the GNA exhibited a large D band peak. D band of GNS is a disorder-activated mode and the intensity of D band is closely related to the number of defects and edges. The relatively intensity ratio of I_D/I_G was calculated to be 0.85, indicating the presence of numerous defects and edges in the GNS support. It is worth mentioning that the Fe catalyst particles in the GNS were completely removed by acid etching as verified by XPS and ICP tests.

3.2. Effects of H_2PtCl_6 Concentration. The effects of the H_2PtCl_6 concentration in the feedstock on the morphology of the catalysts were examined as shown in Figure 2. It can be seen that the Pt NPs were successfully assembled on the GNS. The high-resolution TEM micrographs showed that the Pt NPs were closely adhered to the GNS surface without large aggregates, indicating the strong interaction between the Pt NPs and the support. Based on the TEM micrographs, the Pt cover density (defined as the number of the Pt NPs per unit area) on the GNS support was estimated as shown in Figure 3 (the number of Pt NPs was obtained by counting and the GNS area was estimated by subtracting the blank area from the whole viewing area of TEM images). It can be seen that the Pt cover density on the GNS increased with increasing Pt loading. The Pt cover density in the Pt 20%/GNS catalyst was ca. 42 × 10^3 Pt NPs per μm^2 of GNS while those in the Pt 40%/GNS and Pt 60%/GNS catalysts were 75 and 86 × 10^3 Pt NPs per

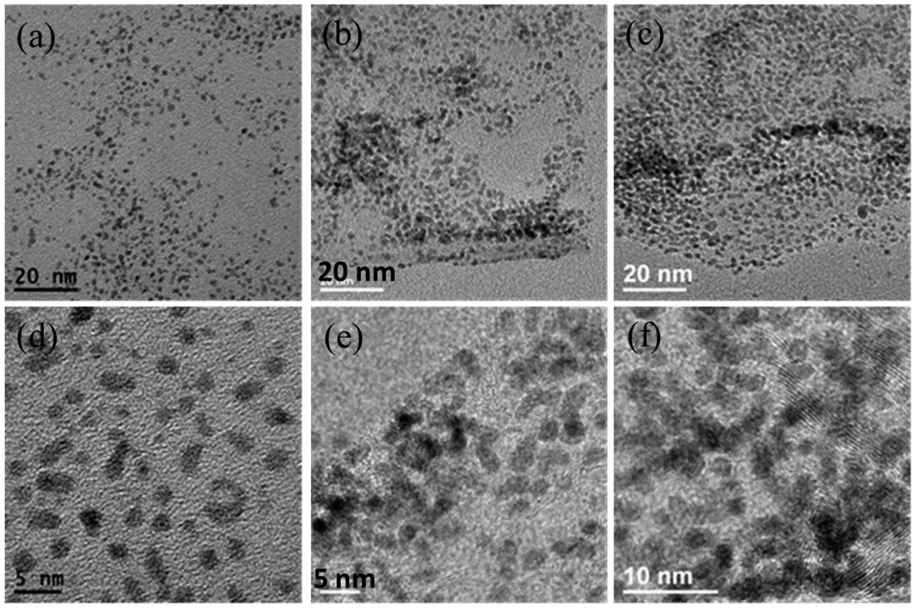

Figure 2. (a–c) Low-magnification and (d–f) high-magnification TEM micrographs of Pt 20%/GNS, Pt 40%/GNS, and Pt 60%/GNS catalyst.

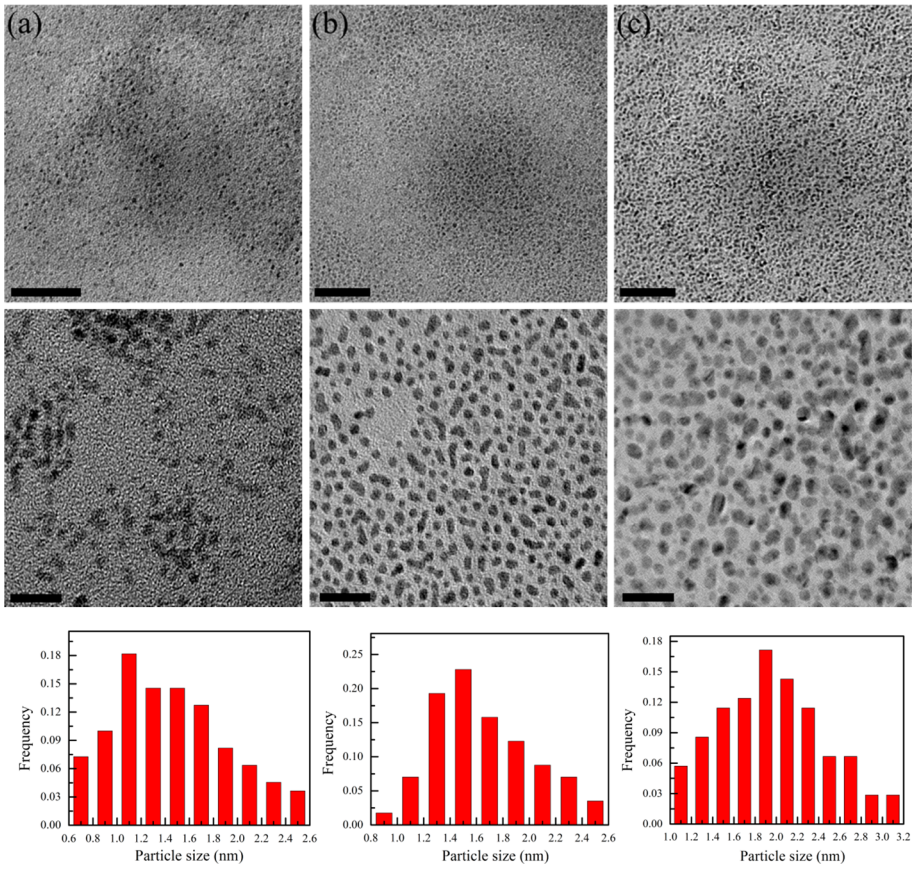

Figure 3. Dependence of cover density and particle size on the Pt loadings of the catalysts (a) Pt 20%/GNS, (b) Pt 40%/GNS, and (c) Pt 60%/GNS. TEM images with (first row) low magnifications (scale bar is 50 nm) and (second row) high magnifications (scale bar is 10 nm), and (third row) histograms of the Pt particle size distribution.

μm^2 of GNS, respectively. One hundred Pt NPs were randomly selected to determine the size distribution and the histograms of Pt NPs in the catalyst were obtained. The Pt NPs in the Pt 20%/GNS catalyst exhibited an average size of 1.4 nm. With increasing Pt loading, the Pt sizes were increased, i.e., the sizes of the Pt NPs in the Pt 40%/GNS and Pt 60%/GNS catalysts were 1.6 and 2.1 nm, respectively. It is noted that some sub-nanometer-scale NPs can be found in the Pt 20%/GNS and Pt 40%/GNS catalyst. It was demonstrated from the TEM micrographs that ultrafine Pt crystals were successfully assembled on the GNS and that the sizes and distribution of Pt NPs in the GNS support were dependent on the

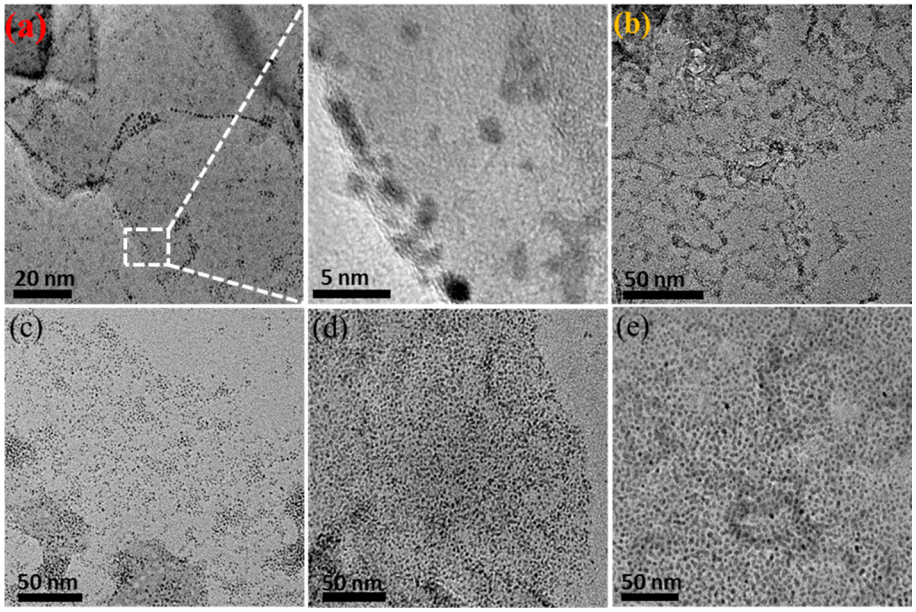

Figure 4. Evolution of Pt NPs in the GNS support at reaction times of (a) 2, (b) 5, (c) 10, (d) 15, and (e) 30 min.

concentration of the H_2PtCl_6 in the feedstock. The elemental composition of the Pt/GNS catalysts was examined by EDX as shown in Figure S1 (see the Supporting Information). The presence of copper signal in the spectra was due to the TEM grid. It was verified that the catalysts consisted of three elements, i.e., platinum, carbon and oxygen, indicating the complete removal of the impurities during the purification process. The Pt NPs were fully crystallized with a face-centered cubic structure as indicated by the lattice fringes shown in the high-resolution TEM micrographs (see Figure S2 in the Supporting Information).

Because the GNS used in this study are derived from CVD process and the GNS surface is quite hydrophobic, the decoration of Pt NPs on the GNS is considered to be very challenging. To the best of our knowledge, the assembly of ultrafine Pt NPs on pristine GNS surface based on a surfactant-free solution process has not been reported. The origin and evolution of the Pt NPs in the GNS support were investigated. The polyol-assisted reduction method has been extensively used for the synthesis of Pt NPs.[41] It has been accepted that the formation of Pt NPs involves two stages, i.e., nucleation and growth stages.[42] The complete separation of the two stages is the prerequisite for the accurate size control of Pt NPs. Surfactants are commonly used to stabilize nuclei and inhibit agglomeration during the synthesis of NPs.[42] Nevertheless, in this study, no surfactant is employed (except that the ethylene glycol used in the synthesis process is claimed to serve as solvent, reduce agent as well as surfactant[43]). It was surmised that the formation of ultrafine Pt NPs could be probably related to the presence of the GNS support. To study the effects of the GNS on the formation of Pt NPs, we conducted comparative experiments. Another two batches of Pt NPs were synthesized in the absence of the GNS support and in the presence of surfactant polyvinylpyrrolidone (PVP). The TEM micrographs of the resulting Pt NPs are shown in Figure S3 in the Supporting Information. It can be seen that the Pt NPs synthesized in the absence of GNS were aggregated due to the high surface energy while highly dispersed Pt NPs were obtained in the presence of PVP, indicating that PVP could effectively prevent the Pt NPs from aggregation. Comparatively, the Pt NPs obtained in the presence of PVP had larger particle sizes (3.6 nm) as compared with those stabilized by GNS support (see Figure S3 in the Supporting Information). These results confirmed that the GNS support plays a key role on the formation of the ultrafine Pt NPs. It is noted that the GNS used in this study contain numerous edges and defects as shown in Figure 1.[40] During the formation of Pt nuclei, the large number of high-energy sites in the GNS could serve as effective heterogeneous nucleation sites to anchor Pt atoms.[44] Consequently, the immobilization of Pt atoms to these sites occurred simultaneously and the concentration of Pt atoms in solution abruptly dropped below the minimum supersaturation, leading to the cease of the nucleation. With a continuous supply of Pt atoms from the reduction of the precursor, the nuclei started to grow via atom addition.[42] During the growth stage, the stabilizing of nuclei through the interaction with GNS was also critical to prevent agglomeration. In the absence of GNS, Pt nuclei were slowly generated through homogeneous nucleation in a long time range, resulting in the concomitance of nucleation and growth during the formation of the Pt NPs.[45] This could probably be the reason for the large sizes and broad size distribution of the Pt NPs obtained in the presence of the PVP.[41] In the absence of GNS and PVP, the substantial stabilizing effects were not available and Pt NPs were prone to aggregate due to the high surface energy as shown in Figure S3a in the Supporting Information.

3.2. Evolution of Pt NPs in GNS Support. The actual Pt content in the resulting catalyst was determined by ICP analyses. The actual Pt weight percentages in the 20%/GNS, 40%/GNS, and 60%/GNS catalyst were 18.6, 32.4, and 44.8%, resulting in a Pt loss of 7, 19, and 25.3% as compared with the nominal Pt content in the feed stock, respectively. The Pt loss could be due to the incomplete reduction of the precursor or it could also occur during the purification and separation process. Supernatants from the separation process were collected and analyzed by TEM as shown in Figure S4a in the Supporting Information. It was indicated that some isolated Pt NPs were observed in the supernatant. To further explore the origin of

the isolated Pt NPs and the evolution of Pt NPs on the GNS, a series of samples were taken at different reaction times during the synthesis of the Pt 40%/GNS hybrid and analyzed by TEM as shown in Figure 4. It clearly showed that the Pt cover density increased with increasing reaction time. At 2 min, the Pt cover density was estimated to be 12×10^3 Pt NPs per μm^2 of GNS. The cover density was increased to 90×10^3 Pt NPs per μm^2 of GNS at 10 min. Meanwhile, the sizes of the Pt NPs were only slightly increased in the initial 10 min (from 1.1 to 1.5 nm). With further increasing reaction time, the Pt cover density was decreased (86×10^3 Pt NPs per μm^2 of GNS), whereas the Pt particle size was abruptly increased to 2.7 nm at 30 min. After the reaction was conducted for 30 min, the product was purified and the resulting supernatant was analyzed again. Very limited Pt NPs were observed in the supernatant as shown in Figure S4b in the Supporting Information.

From the TEM micrographs, it is also interesting to note that Pt NPs were preferentially anchored to the edges and defects of the GNS support. This could be related to the high energy of the edges and defects, which were more effective for immobilizing Pt NPs.[44] Zoval et al.[46] deposited Pt nanocrystals on highly oriented pyrolitic graphite from dilute $PtCl_6^{2-}$ solution. It was first found that Pt NPs nucleate preferentially at edges and point defects of the graphite basal plane. Later, such defect-mediated immobilizing Pt NPs was verified to prevail in Pt/graphene hybrids.[47−51] For instance, Lim et al.[49] studied the interaction of Fe_{13} and Al_{13} clusters with graphene using density functional theory and found the preferential bonding of Fe_{13} and Al_{13} on graphene vacancies, which was attributed to the strong hybridization of the clusters with the sp^2 dangling bonds of neighboring carbons near the vacancy. Experiments also clearly revealed that metal clusters were preferentially located at the defects, e.g., defects, steps and edges using high-resolution TEM.[50,51] During the initial period of the formation of Pt nuclei, Pt atoms (or Pt^{II}−Pt^{I} dimers[52]) were selectively anchored to the high-energy sites in the GNS and homogeneous nucleation of Pt atoms was greatly suppressed. Nevertheless, with the continuous generation of Pt atoms, the high-energy sites were occupied and subsequently the other sites with relatively low energies in the GNS started to act as nucleation sites as indicated by the increases in cover densities.[53] Because the interaction of nuclei with these sites is weak, some of Pt nuclei could be detached from the GNS support, resulting in the presence of tiny Pt NPs in the supernatant after the reaction was conducted for 15 min. It should also be noted that homogeneous nucleation of Pt atoms could not be excluded under this circumstance.[54] With further increasing reaction time, the growth of the Pt NPs and Ostwald ripening occurred. The small NPs in the solution were dissolved for the sake of larger ones immobilized to the GNS support. This was consistent with the results that the sizes of the NPs were increased and the number of Pt NPs in the supernatant was drastically reduced after 30 min.

3.3. XPS Results. XPS was employed to analyze the electronic properties of Pt NPs in the Pt/GNS hybrids. Figure 5 shows the deconvoluted Pt 4f core level XPS spectra and the analysis results are summarized in Table 1. All the spectra were corrected using the C 1s signal located at 284.5 eV. The Pt 4f spectra consisted of two peaks, corresponding to the doublets of Pt 4f7/2 and 4f5/2, respectively. To decompose the spectra, the constraints of equal spin−orbit splitting for Pt 4f peaks in binding energy (BE), peak area and full width at half-maximum (fwhm) were thoroughly considered. The deconvolution of the

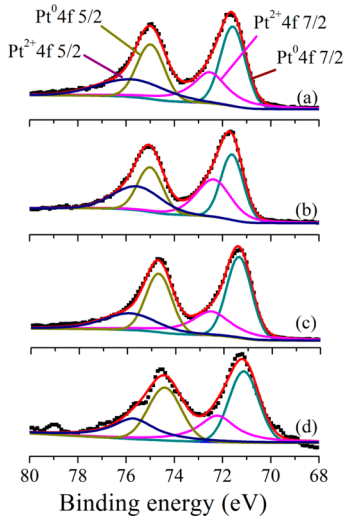

Figure 5. XPS spectra of the Pt 4f core level in the (a) Pt20%/GNS, (b) Pt40%/GNS, and (c) Pt60%/GNS, and (d) Pt synthesized in the presence of PVP.

Pt 4f 5/2 and Pt 4f 7/2 peak yielded two sets of peaks, which could be assigned to Pt^0 and Pt^{2+}, respectively. The concentration ratio between the metallic Pt^0 and Pt^{2+} state was calculated based on the intensity of the corresponding component in the XPS spectra. It was indicated from Table 1 that the Pt60%GNS and Pt-PVP had higher $C_{Pt(0)}/C_{Pt(II)}$ ratios, which could be related to the larger particle sizes and the surface protection of PVP surfactant. The Pt NPs synthesized in the presence of the PVP exhibited a BE of 72.1 eV, which was consistent with the results reported by Nakamura et al.[31] The Pt NPs in the Pt/GNS catalysts showed higher BE and the BEs increased with decreasing Pt loading. This could be explained from the chemical interaction between the Pt NPs and GNS support because of the strong π−d hybridization between the Pt filled d orbitals and carbon p* empty orbitals. This was consistent with the results that the BEs increased with decreasing Pt loading. It was demonstrated that the Pt NPs in the catalysts with lower loadings, such as the Pt 20%/GNS catalyst, were preferentially anchored to the edges and defects of the support (Figure 1). Such strong interaction could shift the BEs to higher energy and affect the d-band structure of the Pt NPs.[31]

3.4. Catalytic Results. The electrochemical catalytic performance of the Pt/GNS hybrids toward methanol oxidation was characterized. A commercial Pt/carbon black (denoted as Pt/C) was used as reference for comparison. Figure 6 shows the CVs of the Pt/GNS and Pt/C catalyst in a solution 1 M H_2SO_4. The electrochemical active surface area (ECSA) of the catalyst was determined using following equation

$$\mathrm{ECSA} = \frac{S/v}{M_{Pt}(210 \times 10^{-6})} \quad (1)$$

where S is the hydrogen adsorption area in the CVs, v is the scanning rate 0.05 V s^{-1}, and M_{Pt} is the Pt mass in the catalyst. The ECSA of the Pt/C catalyst was 63 m^2 g^{-1} Pt, whereas the ECSA values of the 20%/GNS, 40%/GNS, and 60%/GNS catalyst were 91, 77, and 62 m^2 g^{-1} Pt, respectively. It was indicated that the ECSA values of the Pt/GNS catalysts increased with decreasing Pt loading. This could also be

Table 1. Summary of XPS Analysis Results[a]

	Pt 4f7/2 (eV)					Pt 4f5/2 (eV)			
	Pt (0)		Pt (II)			Pt (0)		Pt (II)	
sample	BE	fwhm	BE	fwhm	$C_{Pt(0)}/C_{Pt(II)}$	BE	fwhm	BE	fwhm
Pt 20%/GNS	71.6	1.2	72.5	1.7	1.25	75.0	1.3	75.7	3.3
Pt 40%/GNS	71.5	1.1	72.4	1.7	0.96	75.0	1.2	75.5	2.4
Pt 60%/GNS	71.4	1.2	72.5	2.0	1.43	74.7	1.3	75.9	2.6
Pt - PVP	71.1	1.4	72.2	1.8	1.43	74.4	1.6	75.7	2.1

[a]Estimated BE experimental error was ±0.1 eV. $C_{Pt(0)}/C_{Pt(II)}$ refers to the concentration ratio between the metallic Pt (0) and Pt (II) state.

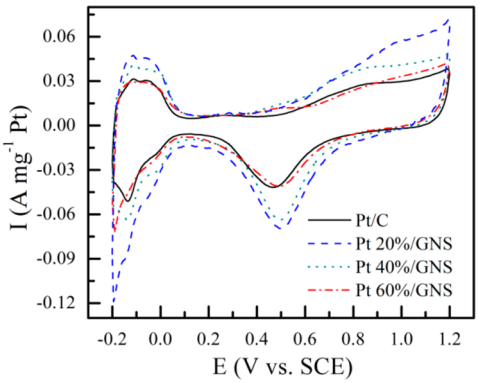

Figure 6. Cyclic voltammetry curves of the catalyst at 25 °C in 1 mol L^{-1} H_2SO_4 with a scan rate of 50 mV s^{-1}.

explained from the effects of Pt loading on the sizes and dispersion of the Pt NPs. With decreasing Pt loading, the size of the Pt NPs decreased. In particular, many Pt subnanoclusters were present in the Pt 20%/GNS catalyst. In addition, the Pt loadings also affected the cover density and the dispersion of the Pt NPs. In the Pt 20%/GNS catalyst, the discrete Pt NPs were uniformly dispersed while some of the Pt NPs in the Pt 40%/GNS and Pt 60%/GNS catalyst were partially overlapped as shown in the TEM micrographs. Therefore, the high ECSA of the Pt 20%/GNS catalyst was attributed to the particle size as well as the dispersion of Pt NPs, which provided more accessible active sites in the Pt/GNS catalyst.

Figure 7 shows the CV curves of methanol electro-oxidation at the Pt/GNS and Pt/C hybrids. The current density shown in the CVs was normalized by the mass of Pt loading. The CVs consisted of two well-defined peaks at the forward and backward scans. The peak at the forward scan was due to the oxidation of methanol molecules while the one at the backward can was related to the oxidation of intermediates. The maximum current densities and the corresponding potentials were determined based in Figure 7a and the results are shown in Table 2. It can be seen that the current densities of the four catalysts followed this order: Pt 20%/GNS > Pt 40%/GNS > Pt/C > Pt 60%/GNS. The Pt 20%/GNS catalyst showed the highest current density of 0.4 A mg^{-1} Pt at the forward scan among the four catalysts. In addition, the onset potential for methanol oxidation at the Pt 20%/GNS catalyst was lowest as shown Figure 7b. It was also shown in Table 2 that the Pt/GNS catalysts exhibited larger ratios of I_F/I_B compared with the Pt/C catalyst, indicating the superior antipoisoning properties of the GNS supported catalysts.[38]

The durability of the catalysts was also evaluated by amperometric measurements. Figure 8 shows chronoamperometric curves for methanol oxidation at a constant potential of 0.6 V. The current densities showed a rapid decay during the initial period because of the poisoning of the intermediate species generated in the oxidation of methanol molecules. The Pt 20%/GNS, Pt 40%/GNS, Pt 60%/GNS and Pt/C catalysts had current densities of 154, 111, 58, and 24 mA mg^{-1} Pt after 1200 s, respectively, which was consistent with the results shown in Table 2. The catalysts deactivated relatively faster in initial times and a plateau was observed with further increasing testing time. Compared with the Pt/C catalyst, the Pt 20%/GNS and Pt 40%/GNS shower better stability while the Pt 60%/GNS catalyst deactivated faster. The catalytic performance of the catalyst could be well correlated with the structural properties. In the Pt/20%/GNS catalyst, the presence of numerous Pt subnano/nanoclusters were consisted of a large number of Pt atoms with low coordination numbers such as edge and corner Pt atoms in the Pt subnanoclusters, which exhibited more active sites and enhanced catalytic activity for methanol oxidation.[55] In addition, the interaction of these Pt subnanoclusters with the graphene edges and surface defects

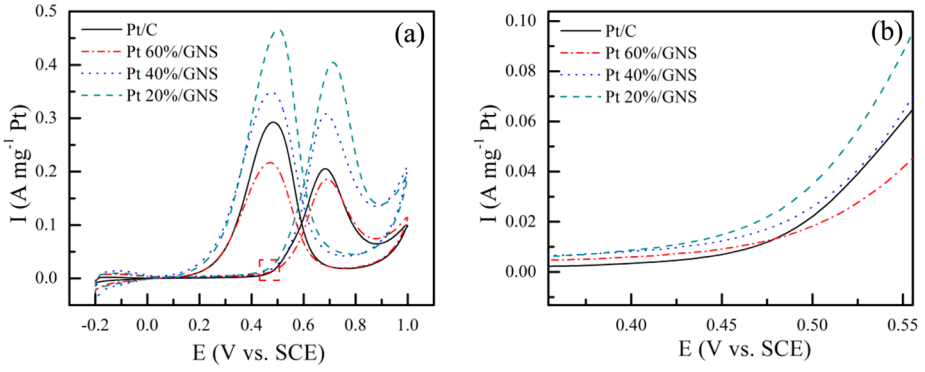

Figure 7. Cyclic voltammetry curves of methanol electro-oxidation on the catalyst at 25 °C in 1 mol L^{-1} methanol−1 mol L^{-1} H_2SO_4 in the potential range of −0.2 to 1.0 V vs SCE with a scan rate of 50 mV s^{-1}. (a) Overview and (b) enlarged view of the spot marked in A.

Table 2. Electrochemical Active Surface Area (ECSA) and Methanol Electro-oxidation Results of the Pt/C and Pt/GNS Catalysts

catalyst	ECSA[a] (m^2 g^{-1} Pt)	E_F[b] (V)	I_F[b] (A mg^{-1} Pt)	E_B[b] (V)	I_B[b] (A mg^{-1} Pt)	I_F/I_B
Pt/C	63	0.68	0.21	0.49	0.29	0.72
Pt 20%/GNS	91	0.71	0.40	0.51	0.47	0.85
Pt 40%/GNS	77	0.69	0.31	0.48	0.35	0.89
Pt 60%/GNS	62	0.69	0.19	0.48	0.22	0.86

[a]Calculated using eq 1 based on Figure 6. [b]Determined based on Figure 7, I_F and I_B are the maximum current density at the forward and backward scan, respectively, and E_F and E_B are the corresponding potentials.

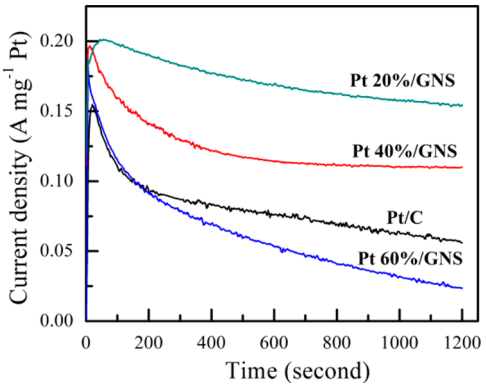

Figure 8. Chronoamperometric curves of the catalysts recorded 25 °C in 1 mol L^{-1} methanol−1 mol L^{-1} H_2SO_4 at a constant potential of 0.6 V.

greatly affected the electronic structure of the Pt cluster as indicated by the XPS results.[31,56] Both these two factors resulted in the superior catalytic activity of the Pt/20%/GNS catalyst. With increasing Pt loading, the particle sizes increased and the support effects of the GNS weakened. Particularly, in the Pt/60%/GNS catalyst, some of the Pt NPs form aggregates on the support and the interaction of the Pt NPs with the GNS support was negligible as stated from the formation process, leading to the lowest activity of the Pt/60%/GNS catalyst. On the basis of these results, it was indicated that the catalytic activity of the Pt/GNS catalyst was highly dependent on the size and dispersion of the Pt NPs. The presence of Pt subnanoclusters and the support effects of the GNS were critical to achieve high catalytic performance.

4. CONCLUSION

Ultrafine Pt NPs were successfully assembled on the hydrophobic GNS surface via a surfactant-free solution process. The high-energy sites, such as edges and defects, in GNS surface served as effective heterogeneous nucleation sites for anchoring and stabilizing of Pt nuclei, resulting in the formation of discrete Pt NPs on the GNS support. The cover densities, sizes and dispersion of Pt NP were closely related to Pt loadings. Lower Pt loadings in the catalysts were favorable for the formation of discrete Pt subnanoclusters and led to strong interaction of Pt NP with the GNS support as confirmed by the XPS results. The electrochemical measurement results showed that, among the four catalysts, the Pt/GNS catalyst with a lowest loading of 20% showed the highest ECSA and current density, which was attributed to the presence of Pt subnano/nanoclusters and the strong chemical interaction of these Pt subnanoclusters with the edges and surface defects of the GNS support. It is demonstrated from this study that the pristine GNS derived from CVD process can be utilized as catalyst support in fuel cells and that the control of the Pt loading in the GNS supported catalyst is the key to achieve high catalytic performance.

■ ASSOCIATED CONTENT

Supporting Information

Figures S1−S5 showing the Raman spectrum and TEM micrographs of the samples. This material is available free of charge via the Internet at http://pubs.acs.org.

■ AUTHOR INFORMATION

Corresponding Authors

*E-mail: feyshen@scut.edu.cn.
*E-mail: xijingyu@gmail.com.

Notes

The authors declare no competing financial interest.

■ ACKNOWLEDGMENTS

We are grateful for the financial support from "the Fundamental Research Funds for the Central Universities (ZB20140003)"

■ REFERENCES

(1) Steele, B. C. H.; Heinzel, A. Materials for Fuel-Cell Technologies. *Nature* **2001**, *414*, 345−352.
(2) Arico, A. S.; Srinivasan, S.; Antonucci, V. DMFCs: from Fundamental Aspects to Technology Development. *Fuel Cells* **2001**, *1*, 133−161.
(3) Neburchilov, V.; Martin, J.; Wang, H. J.; Zhang, J. J. A Review of Polymer Electrolyte Membranes for Direct Methanol Fuel Cells. *J. Power Sources* **2007**, *169*, 221−238.
(4) Jiang, Q. A.; Jiang, L. H.; Hou, H. Y.; Qi, J.; Wang, S. L.; Sun, G. Q. Promoting Effect of Ni in PtNi Bimetallic Electrocatalysts for the Methanol Oxidation Reaction in Alkaline Media: Experimental and Density Functional Theory Studies. *J. Phys. Chem. C* **2010**, *114*, 19714−19722.
(5) Nam, K. W.; Song, J.; Oh, K. H.; Choo, M. J.; Park, H.; Park, J. K.; Choi, J. W. Monodispersed PtCo Nanoparticles on Hexadecyltrimethylammonium Bromide Treated Graphene as an Effective Oxygen Reduction Reaction Catalyst for Proton Exchange Membrane Fuel Cells. *Carbon* **2012**, *50*, 3739−3747.
(6) Xu, C. X.; Li, Q.; Liu, Y. Q.; Wang, J. P.; Geng, H. R. Hierarchical Nanoporous PtFe Nlloy with Multimodal Size Distributions and Its Catalytic Performance Toward Methanol Electrooxidation. *Langmuir* **2012**, *28*, 1886−1892.
(7) Wang, S. Y.; Wang, X.; Jiang, S. P. PtRu Nanoparticles Supported on 1-aminopyrene-Functionalized Multi-walled Carbon Nanotubes and Their Electrocatalytic Activity for Methanol Oxidation. *Langmuir* **2008**, *24*, 10505−10512.
(8) Okaya, K.; Yano, H.; Uchida, H.; Watanabe, M. Control of Particle Size of Pt and Pt Alloy Electrocatalysts Supported on Carbon Black by the Nanocapsule Method. *ACS Appl. Mater. Interfaces* **2010**, *3*, 888−2010.

(9) Lu, Y. Z.; Jiang, Y. Y.; Chen, W. Graphene Nanosheet-Tailored PtPd Concave Nanocubes with Enhanced Electrocatalytic Activity and Durability for Methanol Oxidation. *Nanoscale* **2014**, *6*, 3309−3315.
(10) Hayden, B. E. Particle Size and Support Effects in Electrocatalysis. *Acc. Chem. Res.* **2013**, *46*, 1858−1866.
(11) Cao, M. N.; Wu, D. S.; Cao, R. Recent Advances in the Stabilization of Platinum Electrocatalysts for Fuel-Cell Reactions. *ChemCatchem.* **2014**, *6*, 26−45.
(12) Moore, A. D.; Holmes, S. M.; Roberts, E. P. L. Evaluation of Porous Carbon Substrates as Catalyst Supports for the Cathode of Direct Methanol Fuel Cells. *RSC Adv.* **2012**, *2*, 1669−1674.
(13) Maiyalagan, T.; Alaje, T. O.; Scott, K. Highly Stable Pt-Ru Nanoparticles Supported on Three-Dimensional Cubic Ordered Mesoporous Carbon (Pt-Ru/CMK-8) as Promising Electrocatalysts for Methanol Oxidation. *J. Phys. Chem. C* **2012**, *116*, 2630−2638.
(14) Tian, Z. Q.; Jiang, S. P.; Liang, Y. M.; Shen, P. K. Synthesis and Characterization of Platinum Catalysts on Multi-walled Carbon Nanotubes by Intermittent Microwave Irradiation for Fuel Cell Applications. *J. Phys. Chem. B* **2006**, *110*, 5343−5350.
(15) Xi, J. Y.; Wang, J. S.; Yu, L. H.; Qiu, X. P.; Chen, L. Q. Facile Approach to Enhance the Pt Utilization and CO-tolerance of Pt/C Catalysts by Physically Mixing with Transition-Metal Oxide Nanoparticles. *Chem. Commum.* **2007**, *16*, 1656−1658.
(16) Santasalo-Aarnio, A.; Borghei, M.; Anoshkin, I. V.; Nasibulin, A. G.; Kauppinen, E. I.; Ruiz, V.; Kallio, T. Durability of Different Carbon Nanomaterial Supports with PtRu Catalyst in a Direct Methanol Fuel Cell. *Int. J. Hydrogen Energy* **2012**, *37*, 3415−3424.
(17) Chang, H. X.; Wu, H. K. Graphene-Based Nanocomposites: Preparation, Functionalization, and Energy and Environmental Applications. *Energy Environ. Sci.* **2013**, *6*, 3483−3507.
(18) Huang, C. C.; Li, C.; Shi, G. Q. Graphene Based Catalysts. *Energy Environ. Sci.* **2012**, *5*, 8848−8868.
(19) Antolini, E. Carbon Supports for Low-Temperature Fuel Cell Catalysts. *Appl. Catal., B* **2009**, *88*, 1−24.
(20) Sharma, S.; Pollet, B. G. Support Materials for PEMFC and DMFC Electrocatalysts-A Review. *J. Power Sources* **2012**, *208*, 96−119.
(21) Long, N. V.; Yang, Y.; Thi, C. M.; Minh, N. V.; Cao, Y. Q.; Nogami, M. The Development of Mixture, Alloy, and Core-Shell Nanocatalysts with Nanomaterial Supports for Energy Conversion in Low-Temperature Fuel Cells. *Nano Energy* **2013**, *2*, 636−676.
(22) Yang, J.; Xie, Y.; Wang, R. H.; Jiang, B. J.; Tian, C. G.; Mu, G.; Yin, J.; Wang, B.; Fu, H. G. Synergistic Effect of Tungsten Carbide and Palladium on Graphene for Promoted Ethanol Electrooxidation. *ACS Appl. Mater. Interfaces* **2013**, *5*, 6571−6579.
(23) Antolini, E. Graphene as a New Carbon Support for Low-Temperature Fuel Cell Catalysts. *Appl. Catal., B* **2012**, *123*, 52−68.
(24) Zhao, S.; Shao, Y. Y.; Yin, G. P.; Lin, Y. H. Recent Progress in Nanostructured Electrocatalysts for PEM Fuel Cells. *J. Mater. Chem. A* **2013**, *1*, 4631−4641.
(25) Xu, C.; Wang, X.; Zhu, J. W. Graphene-Metal Particle Nanocomposite. *J. Phys. Chem. C* **2008**, *112*, 19841−19845.
(26) Liu, M. M.; Zhang, R. Z.; Chen, W. Graphene-Supported Nanoelectrocatalysts for Fuel Cells: Synthesis, Properties and Applications. *Chem. Rev.* **2014**, DOI: 10.1021/cr400523y.
(27) Huang, H. J.; Wang, X. Recent Progress on Carbon-Based Support Materials for Eletrocatalysts of Direct Methanol Fuel Cells. *J. Mater. Chem. A* **2014**, *2*, 6249−6670.
(28) Xu, P. F.; Dong, L. F.; Neek-Amal, M.; Ackerman, M. L.; Yu, J. H.; Barber, S. D.; Schoelz, J. K.; Qi, D. J.; Xu, F. F.; Thibado, P. M.; Peeters, F. M. Self-Organized Platinum Nanoparticles on Freestanding Graphene. *ACS Nano* **2014**, *8*, 2697−2703.
(29) Ren, F. F.; Wang, H. W.; Zhai, C. Y.; Zhu, M. S.; Yue, R. R.; Du, Y. K.; Yang, P.; Xu, J. K.; Lu, W. S. Clean Method for the Synthesis of Reduced Graphene Oxide-Supported PtPd Alloys with High Electrocatalytic Activity for Ethanol Oxidation in Alkaline Medium. ACS. *ACS Appl. Mater. Interfaces* **2014**, *6*, 3607−3614.
(30) Kung, C. C.; Lin, P. Y.; Xue, Y. H.; Akolkar, R.; Dai, L. M.; Yu, X.; Liu, C. C. Three Dimensional Graphene Foam Supported Platinum-Ruthenium Bimetallic Nanocatalysts for Direct Methanol and Direct Ethanol Fuel Cell Applications. *J. Power Sources* **2014**, *256*, 329−335.
(31) Nakamura, J. J.; Kondo, T. Support Effects of Carbon on Pt Catalysts. *Top Catal.* **2013**, *56*, 1560−1568.
(32) Yoo, E. J.; Okata, T.; Akita, T.; Kohyama, M.; Nakamura, J.; Honma, I. Enhanced Electrocatalytic Activity of Pt Subnanoclusters of Graphene Nanosheets Surface. *Nano Lett.* **2009**, *6*, 2252−2259.
(33) Sharma, S.; Ganguly, A.; Papakonstantinou, P.; Miao, X. P.; Li, M. X.; Hutchison, J. L.; Delichatsios, M.; Ukleja, S. Rapid Microwave Synthesis of CO Tolerant Reduced Graphene Oxide-Supported Platinum Electrocatalysts for Oxidation of Methanol. *J. Phys. Chem. C* **2010**, *14*, 19459−19466.
(34) Siburian, R.; Kondo, T.; Nakamura, J. Size Control to a Subnanometer Scale in Platinum Catalysts on Graphene. *J. Phys. Chem. C* **2013**, *117*, 3635−3645.
(35) Lu, Y. Z.; Jiang, Y. Y.; Wu, H. B.; Chen, W. Nano-PtPd Cubes on Graphene Exhibit Enhanced Activity and Durability in Methanol Electrooxidation after CO Stripping-Cleaning. *J. Phys. Chem. C* **2013**, *117*, 2926−2938.
(36) Qiu, J. D.; Wang, G. C.; Liang, R. P.; Xia, X. H.; Yu, H. W. Controllable Deposition of Platinum Nanoparticles on Graphene as an Electrocatalyst for Direct Methanol Fuel Cells. *J. Phys. Chem. C* **2011**, *115*, 15639−15645.
(37) Kundu, P.; Nethravathi, C.; Deshpande, P. A.; Rajamathi, M.; Madras, G.; Ravishankar, N. Ultrafast Microwave-Assisted Route to Surfactant-Free Ultrafine Pt Nanoparticles on Graphene: Synergistic Co-reduction Mechanism and High Catalytic Activity. *Chem. Mater.* **2011**, *23*, 2772−2780.
(38) Qian, W.; Hao, R.; Zhou, J.; Eastman, M.; Manhat, B. A.; Sun, Q.; Goforth, A. M.; Jiao, J. Exfoliated Graphene-Supported Pt and Pt-based Alloys as Electrocatalysts for Direct Methanol Fuel Cells. *Carbon* **2013**, *52*, 595−604.
(39) Shan, C. S.; Tang, H.; Wong, T. L.; He, L. F.; Lee, S. T. Facile Synthesis of a Large Quantity of Graphene by Chemical Vapor Deposition: an Advanced Catalyst Carrier. *Adv. Mater.* **2012**, *24*, 2491−2495.
(40) Shen, Y.; Lua, A. C. A Facile Method for the Large-Scale Continuous Synthesis of Graphene Sheets Using a Novel Catalyst. *Sci. Rep.* **2013**, *3*, 3037.
(41) Thurston, H.; Chen, J. Y.; Xia, Y. N. Polyol Synthesis of Platinum Nanoparticles: Control of Morphology with Sodium Nitrate. *Nano Lett.* **2004**, *4*, 2367−2371.
(42) Xia, Y. N.; Xiong, Y. J.; Lim, B.; Skrabalak, S. E. Shape-Controlled Synthesis of Metal Nanocrystals: Simple Chemistry Meets Complex Physics? *Angew. Chem., Int. Ed.* **2009**, *48*, 60−103.
(43) Size-Selected Synthesis of PtRu Nano-Catalysts: Reaction and Size Control Mechanism . *J. Am. Chem. Soc.* **2004**, *126*, 8028−8037.
(44) Kvande, I.; Zhu, J.; Zhao, T. J.; Hammer, N.; Rønning, M.; Raaen, S.; Walmsley, J. C.; Chen, D. Importance of Oxygen-Free Edge and Defect Sites for the Immobilization of Colloidal Pt Oxide Particles with Implications for the Preparation of CNF-Supported Catalysts. *J. Phys. Chem. C* **2010**, *114*, 1752−1762.
(45) Fievet, F.; Lagier, J. P.; Blin, B. Homogeneous and Heterogeneous Nucleations in the Polyol Process for the Preparation of Micron and Submicron Size Metal Particles. *Solid State Ionics* **1989**, *32/33*, 198−205.
(46) Zoval, J. V.; Lee, J.; Gorer, S.; Penner, R. M. Electrochemical Preparation of Platinum Nanocrystallites with Size Selectivity on Basal Plane Oriented Graphite Surfaces. *J. Phys. Chem. B* **1998**, *102*, 1166−1175.
(47) Fampiou, I.; Ramasubramaniam, A. Binding of Pt Nanoclusters to Point Defects in Graphene: Adsorption, Morphology, and Electronic Structure. *J. Phys. Chem. C* **2012**, *116*, 6543−6555.
(48) Logsdail, A. J.; Akola, J. Interaction of Au_{16} Nanoclusters with Defects in Supporting Graphite: A Density-Functional Study. *J. Phys. Chem. C* **2011**, *115*, 15240−15250.
(49) Lim, D. H.; Negreira, A. S.; Wilcox, J. DFT Studies on the Interaction of Defective Graphene-Supported Fe and Al Nanoparticles. *J. Phys. Chem. C* **2011**, *115*, 8961−8970.

(50) Rodriguez-Manzo, J.; Cretu, O.; Banhart, F. Tapping of Metal Atoms in Vacancies of Carbon Nanotubes and Graphene. *ACS Nano* **2010**, *4*, 3422−3428.
(51) Moldovan, M. S.; Bulou, H.; Dappe, Y. J.; Janowska, I.; Begin, D.; Pham-Huu, C.; Ersen, O. On the Evolution of Pt Nanoparticles on Few-Layer Graphene Supports in the High-Temperature Range. *J. Phys. Chem. C* **2012**, *116*, 9274−9282.
(52) Walmsley, J. C.; Chen, D.; Ciacchi, L. C.; Pompe, W.; Vita, A. D. Initial Nucleation of Platinum Clusters after Reduction of K_2PtCl_4 in Aqueous Solution: a First Principles Study. *J. Am. Chem. Soc.* **2001**, *123*, 7371−7380.
(53) Formo, E.; Camargo, P. H. C.; Lim, B.; Jiang, M. J.; Xia, Y. N. Functionalization of ZrO2 Nanofibers with Pt Nanostructures: the Effects of Surface Roughness on Nucleation Mechanism and Morphology control. *Chem. Phys. Lett.* **2009**, *476*, 56−61.
(54) Kashchiev, D.; van Rosmalen, G. M. Review: Nucleation in Solutions Revisited. *Cryst. Res. Technol.* **2003**, *38*, 555−574.
(55) Sun, S. H.; Zhang, G. X.; Gauquelin, N.; Chen, N.; Zhou, J. G.; Yang, S. L.; Chen, W. F.; Meng, X. B.; Geng, D. S.; Banis, M. N.; Li, R. Y.; Ye, S. Y.; Knights, S.; Botton, G. A.; Sham, T. K.; Sun, X. L. Single-Atom Catalysis Using Pt/Graphene Achieved through Atomic Layer Deposition. *Sci. Rep.* **2013**, *3*, 1775.
(56) Kim, Y. A.; Hayashi, T.; Kim, J. H.; Endo, M. Important Roles of Graphene Edges in Carbon-Based Energy Storage Devices. *J. Energy Chem.* **2013**, *22*, 183−194.